GPS Solutions (2024) 28:62
https://doi.org/10.1007/s10291-023-01602-6

ORIGINAL ARTICLE

On the estimation of scintillation severity using background F-region peak densities: description and example results using GOLD observations

J. Sousasantos[1] · F. S. Rodrigues[1] · A. O. Moraes[2] · R. W. Eastes[3] · J. F. G. Monico[4]

Received: 13 March 2023 / Accepted: 12 December 2023 / Published online: 18 January 2024

Abstract
Amplitude scintillations in Global Navigation Satellite System (GNSS) signals are commonly observed at low latitudes and are frequently associated with equatorial plasma bubbles. The scintillation severity is enhanced around the equatorial ionization anomaly, being controlled, in great part, by the ionospheric F-region background density. This work proposes the use of collocated observations from space-based and distributed ground-based monitors to quantify the relationship between the background F-region peak electron density (NmF2) and scintillation severity. To test the proposed approach and its feasibility, NmF2 observations from the Global-scale Observations of the Limb and Disk (GOLD) instrument and L-band scintillation measurements made by a network of GNSS-based scintillation monitors were used. The observations were made at low latitudes in October 2022, during the ascending phase of solar cycle 25. Results show the influence of background NmF2 on scintillation severity. The results also quantify the control of the latitudinal distribution of maximum S_4 values [$S_{4\ (\max)}$] by the latitudinal variation of NmF2. An empirical relationship between NmF2 and $S_{4\ (\max)}$ for a given local time was also derived for the time of GOLD observations. An application of the empirical relationship between NmF2 and maximum S_4 is illustrated with regional (Brazilian) maps of potential maximum scintillation severity using GOLD-like data. Encouraging results include showing that $S_{4\ (\max)}$ can be estimated from independent observations for a distinct longitude sector, but similar solar flux and season. Future studies will address to what extent the relationship between NmF2 and $S_{4\ (\max)}$ varies for different geophysical conditions.

Keywords GNSS · Ionospheric scintillation · Scintillation severity · Scintillation prediction · Space weather

Introduction

Radio signals propagating through the earth's upper atmosphere are known to be affected by the ionospheric plasma (Yeh and Liu 1982). One of the most significant effects is ionospheric scintillation, which can be described as amplitude and/or phase fluctuations caused by ionospheric density (permittivity) irregularities. Severe scintillation events are of particular concern for applications that rely on Global Navigation Satellite System (GNSS) signals since they can cause loss of lock and cycle slips, affecting the performance of GNSS receivers (Yousuf et al. 2023). Scintillation is more intense and longer-lasting over low latitudes (Aarons et al. 1982). The condition that leads to ionospheric scintillation is the existence of plasma density irregularities. Given the importance of scintillation for fundamental and applied studies, extensive research efforts have been dedicated to estimating scintillation severity from ionospheric measurements.

At low latitudes, plasma density irregularities responsible for L-band (1–2 GHz) scintillation are associated with the so-called Equatorial Plasma Bubbles (EPBs), which develop at nighttime due to the generalized Rayleigh–Taylor instability (Kelley et al. 1981). These EPBs originate in

✉ J. Sousasantos
jonas.ssts@utdallas.edu

1 Willian B. Hanson Center for Space Sciences, The University of Texas at Dallas, Richardson, TX, USA

2 Instituto de Aeronáutica e Espaço (IAE), São José dos Campos, SP, Brazil

3 Laboratory for Atmospheric and Space Physics, University of Colorado Boulder, Boulder, CO, USA

4 Universidade Estadual Paulista Júlio de Mesquita Filho (UNESP), Presidente Prudente, SP, Brazil

the bottomside F-region at the magnetic equator and evolve vertically. The EPBs and associated ionospheric irregularities are aligned with the geomagnetic field and, therefore, map to low latitudes as EPBs gain altitude. Prediction of the occurrence of EPBs and specification of their spatiotemporal evolution are still subjects of ongoing research efforts. Several studies, however, have already shown that scintillation events associated with EPBs are more severe at low latitudes compared to the regions very close to the dip equator (de Paula et al. 2003; Moraes et al. 2018a; Salles et al. 2021; Sousasantos et al. 2022b). That has been commonly explained in terms of the expected variation in the amplitude of plasma perturbations (ΔN), which are directly related to scintillation intensity (Yeh and Liu 1982). As the EPB depletions grow in latitude, they reach higher background densities associated with the Equatorial Ionization Anomaly (EIA) crests, creating plasma perturbations with larger amplitudes. The importance of the background plasma density is also mentioned in studies using measurements made at conjugate geomagnetic sites. They show that the same EPB event can cause distinct scintillation magnitudes at the two sites because of differences in background densities (Sousasantos et al. 2022a). Also, strong scintillation can be experienced at low and mid latitudes due to enhanced ionospheric densities caused by space weather events (Rodrigues et al. 2021; Sousasantos et al. 2023). Therefore, one can expect a relationship between scintillation severity, as expressed by the S_4 scintillation index, and the background ionospheric density, expressed by the F-region peak electron density (NmF2). S_4 is an index commonly used in fundamental and applied scintillation studies. It quantifies the amplitude scintillation and can be described as the standard deviation of the signal intensity normalized by its mean (Briggs and Parkin 1963; Yeh and Liu 1982).

Whalen (2009) examined the relationship between NmF2 and S_4 values. In his work, NmF2 values were obtained from Digisonde measurements (Reinisch et al. 1989). The amplitude scintillation (S_4 indices for 1.5 GHz signals) was obtained from a SCINDA network station (Basu and Groves 2001) that recorded transmissions from the Marisat satellite. The measurements were made at Ascension Island, near the EIA peak (dip latitude 19.76°S at the time). A total of 11 days of measurements from the period between March 13 and 31, 2001, when scintillation was detected, was analyzed. During scintillation events, NmF2 measurements made by Digisondes are typically not available due to the occurrence of spread-F. To overcome this lack of reliable data, Whalen (2009) employed a polynomial fit of the NmF2 as a function of local time to obtain values of background peak densities. Subsequently, he compared values of maximum S_4 [$S_{4\,(\max)}$] with the corresponding NmF2 values and showed a clear relationship between $S_{4\,(\max)}$ and NmF2. Surprisingly, additional studies have not yet taken advantage of Whalen (2009) approach and his encouraging results. This could be, at least in part, because collocated NmF2 and S_4 measurements have been limited.

Advances in distributed instrumentation and measurements motivated this revisit of Whalen's (2009) work. More specifically, it is proposed here that the use of collocated and spatially distributed observations of scintillation and NmF2 is suitable to evaluate, more comprehensively than previously possible, the relationship between these parameters. It is also demonstrated that it is possible to generate risk assessments of scintillation severity based on background F-region density estimates. Examples that illustrate the proposed approach and its feasibility are presented. These examples use simultaneous and collocated measurements of NmF2, made by the Global-scale Observations of the Limb and Disk (GOLD) (Eastes et al. 2017), and of scintillation, made by a set of GNSS-based monitors. The main results are presented and discussed in detail.

Stations, instruments, and methods

To expand the work of Whalen (2009) and better evaluate the relationship between the background ionospheric F-region densities and the scintillation severity, collocated and spatially distributed measurements of NmF2 and S_4 were used. Data from GOLD (Eastes et al. 2017; Eastes et al. 2019) and ground-based scintillation monitors over the Brazilian region were analyzed to illustrate the proposed approach and evaluate its feasibility. The period selected for this analysis covers October 1–30, 2022. During this period equatorial spread-F is observed in the Brazilian sector (e.g., Sobral et al. 2002) and scintillation starts early in the night (Sousasantos et al. 2018). The dataset was inspected night-by-night to ensure that the observations used captured scintillation over a wide range of magnitudes and dip latitudes. More specifically, the range of observed S_4 values were inspected to avoid that only weak scintillation (small S_4 values) was present in the entire dataset or in only a few nights. Signatures of EPBs in both, scintillation and GOLD data were observed in 29 out of 30 consecutive nights in this study. The solar flux index (F10.7) varied between 104 and 163 sfu (see Figure_S1 in the supplementary material). These conditions favored a wide range of scintillation intensities.

GNSS-based measurements of scintillation severity

Scintillation data were obtained from the CIGALA/CALIBRA network, currently modernized and managed by the INCT GNSS NavAer project (Monico et al. 2013, 2022, de Paula et al. 2023). The scintillation measurements were made by Septentrio multi-frequency GNSS reference receivers (model PolaRx5S). Several studies in the past used high-rate data from these receivers (e.g., Moraes et al. 2018b;

Table 1 Geographic coordinates and dip latitudes of the GNSS ground-based stations used in this work

Station	STNT	STSN	STCB	PRU2	STSH	POAL	STBR
Geographic longitude	35.19°W	55.54°W	56.07°W	51.41°W	54.34°W	51.12°W	49.21°W
Geographic latitude	5.84°S	11.83°S	15.55°S	22.12°S	24.85°S	30.07°S	28.83°S
Dip latitude	12.10°S	7.15°S	10.07°S	17.80°S	18.37°S	23.55°S	23.71°S

Moraes et al. 2018c; Vani et al. 2019, 2021; Affonso et al. 2022). In this work, the L1 frequency (1575.42 MHz) was used. The ionospheric amplitude scintillation was evaluated using the index S_4 (Yeh and Liu 1982):

$$S_4 = \sqrt{\frac{\langle I^2 \rangle - \langle I \rangle^2}{\langle I \rangle^2}} \quad (1)$$

where the intensity of the signal is represented by I, and the angle brackets correspond to temporal averages over 60 s intervals. Only data from satellites with high elevation angles ($\geq 45°$) were used. The elevation angle constraint has two purposes. First, it guarantees that plasma density deviations over the stations dominate over other possible factors regulating the observed scintillation severity (Affonso et al. 2022; Sousasantos et al. 2022b). In addition to that, it avoids possible contamination from multipath effects. The Ionospheric Pierce Points (IPP) for all the stations and for all the datasets are assumed at 350 km of altitude. Also, although studies show possible code interference in Global Positioning System (GPS) observables using high-latitude stations (Flynn et al. 2019), these values, in terms of S_4, are typically very small and negligible when discussing low-latitude scintillation (S_4 reaching up to 1.2). As an extra caution, however, all the data for all the nights were inspected to ensure the absence of multipath and outliers. Moreover, data samples exhibiting a cycle slip counter parameter below 60 s were identified as instances of cycle slip occurrences (Moraes et al. 2017), these samples were subsequently excluded from the dataset used in the analysis.

The data used in this study is from 6 scintillation monitors located along nearly the same magnetic meridian, but at different magnetic dip latitudes. Therefore, it was possible to study the variation of scintillation associated with the same field-aligned EPB structure. Table 1 lists the geographic coordinates and dip latitudes of these 6 ground stations and one additional station (STNT) used to test the proposed approach. The International Geomagnetic Reference Field (IGRF-13) (Alken et al. 2021) was used to calculate the geomagnetic dip latitudes and magnetic meridians.

Figure 1 shows the location of the 7 stations used (colored "x" markers) and their field-of-view (circular dashed lines) for 45° elevation angle masks and considering the IPPs at 350 km of altitude. As mentioned earlier, the station at the eastern coast of Brazil (STNT) was used to test the approach proposed in this work.

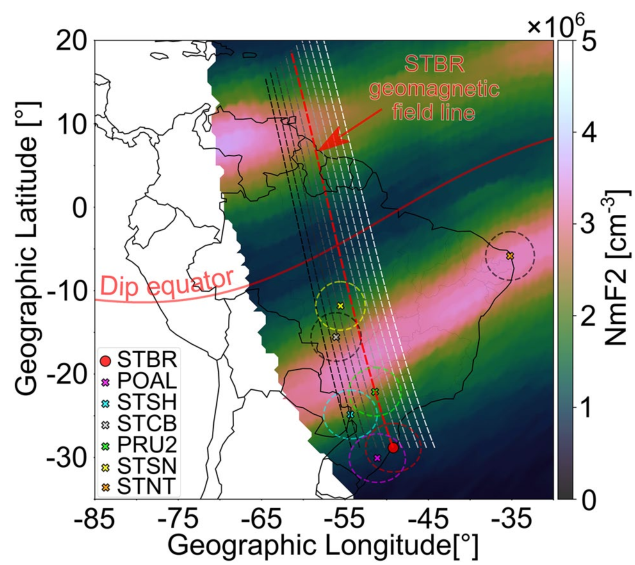

Fig. 1 Location of the GNSS ground-based stations used in this work (x markers). Elevation masks at 45° are indicated by circular dashed lines for each station. Grey dashed lines describe the location of 11 magnetic field lines (magnetic meridians) spaced by 1° in longitude. The red dashed line corresponds to the projection of the geomagnetic field line with the southern footpoint starting at 350 km over STBR (the station with larger dip latitude). A map of NmF2 produced with GOLD data is also shown, with values detailed by the color bar at the right

GOLD measurements of background F-region densities

To evaluate the relationship between S_4 values and the background F-region peak densities, the GOLD level 2 NMAX (F-region peak density, i.e., NmF2) geolocated data were used. These data products are derived from the two independent channels of the GOLD high-resolution far-ultraviolet imaging spectrograph, that make measurements (geolocated) over the southern and northern hemispheres, sequentially. The errors associated with these measurements are less than 10% (McClintock et al. 2020). Scans covering the region of the 6 ground-based scintillation monitors (STBR, POAL, STSH, STCB, PRU2, and STSN) are available for universal times (UT) between 23:11 UT and 00:38 UT, corresponding to local times (LT) between approximately 19:35 LT–21:00 LT. The Balneário Rincão station (STBR) was used as a reference. The geomagnetic field line starting at 350 km (IPP altitude) over STBR (red dashed line) is traced using the IGRF-13.

The geographic latitude of STBR was used to trace field lines around that of STBR (black-to-white dashed lines in Fig. 1). Each of these 10 additional field lines are spaced by 1°, covering about 10° in geographic longitude (or, equivalently, about 40 min). The S_4 data from all the available GNSS constellations were gathered from the time of the first GOLD scan over STBR up to the last time of observation in the final scan (from 23:11 UT and 00:38 UT, as mentioned).

It must be emphasized that the quantity of interest from GOLD is the background NmF2 and not the density values within EPBs. This is because the target is to quantify the relationship between background F-region peak density and the severity of scintillation if an EPB were to be present in the signal path. However, low density values associated with EPB depletions are often present in the GOLD NMAX images. In addition, each pair of GOLD scans from the northern and southern hemispheres overlap to each other over certain regions around the geographic equator. To reduce EPB signatures and to have univocal background NMAX values, consecutive scans were used to create a regularly gridded longitude × latitude map of the background NmF2. The maximum value of NmF2 was calculated for each grid cell (0.5° × 0.5°) and a version of the "rolling-ball" algorithm (Sternberg 1983; Lou et al. 2013), commonly used to remove ionospheric depletions (Smith and Heelis 2018a, b), was applied, resulting in a map representative of the background peak electron density for the time interval of interest. An example of such a map (for October 23, 2022) produced using GOLD data and the procedure described above is shown in Fig. 1.

Results and discussion

Results of the analyses of NmF2 and S_4 measurements are presented and discussed in the following sections. First, latitudinal profiles of these parameters are shown, confirming control of scintillation severity by the background F-region peak density. Next, the relationship between maximum S_4 and background NmF2 for a specific LT and longitude sector is quantified using scintillation and NmF2 measurements for the same coordinates. Then, the application of this relationship to predict maximum bounds for S_4 based on GOLD NmF2 measurements is presented and discussed. Finally, assuming that the derived relationship holds for other LTs and longitudes (but similar season and solar flux), the generation of maps of scintillation severity risk based on measurements such as those provided by GOLD is illustrated.

On the dependence of the severity of the ionospheric scintillation on the NmF2 values

To perform the analyses presented in this study only data from GNSS satellites with high elevation angles (≥ 45°) are considered, such that the NMAX (NmF2) data from GOLD can be suitably compared with S_4 over approximately the same region. High elevation angle measurements also ensure that only data from nearly the same magnetic meridian are used. Additionally, with a high elevation angle, the effect of the electron density deviation on the generation of ionospheric scintillation will dominate over other possible contributions (Affonso et al. 2022; Sousasantos et al. 2022b). With the considerations above, a direct relation between NmF2 and the S_4 severity can be examined and estimated.

The first analysis performed was designed to verify how both quantities, NmF2 and S_4, vary with dip latitude and to demonstrate the resemblance of their magnitudes along the magnetic meridian. After building the NmF2 2D representation in the longitude × latitude grid using the procedure described in the previous section, the NmF2 values over the geomagnetic field lines exhibited in Fig. 1 were selected. Therefore, 11 latitudinal profiles of NmF2 covering the region of the 6 scintillation monitors were obtained for each night. Since the monitors were located between the geomagnetic equator and the dip latitude of 23.71° S, only the southern portions of the NmF2 profiles were needed in this analysis.

Figure 2 shows the NmF2 profiles at the location of the field lines considered here. More specifically, these are the background ionosphere NmF2 values at the coordinates of the field lines shown in Fig. 1. The NmF2 profiles are displayed with the same colors (i.e., black-to-gray), except for the field line over STBR, which is depicted by the thicker green line (instead of using red as in Fig. 1) to avoid overlaps with the scatter plot. Four nights (days of year 275, 297, 298, and 302 of 2022) were used to exemplify the general trend in the results. The NmF2 profiles are displayed according to the dip latitudes in the southern hemisphere, and their values are related to the vertical axis in the left. The S_4 indices recorded by the 6 ground-based scintillation monitors were also organized according to the dip latitudes and are exhibited in the panels of Fig. 2 with blue/red circles indicating smaller/larger values, as described by the vertical axis at the right-hand side.

According to the curves in Fig. 2, the NmF2 magnitudes and the dip latitudes of the peak of the NmF2 profiles change from night-to-night. These aspects are coherent and agree with theoretical and observational evidence found in the past (Basu et al. 2009; Batista et al. 2011; Khadka et al. 2018). Nevertheless, a noteworthy aspect is the strong resemblance between the trend in the scintillation severity and the NmF2 curves. It is evident that the

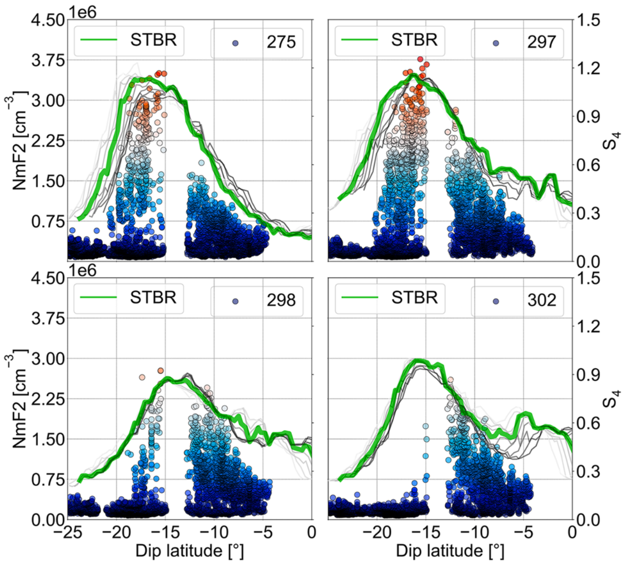

Fig. 2 Profiles of NmF2 (black-to-gray and green curves) and S_4 (blue/red circles) according to dip latitudes for 4 different nights in 2022 (indicated on the top right corner of each panel). The NmF2/S_4 values are exhibited by the vertical left/right axes. The time interval covered 23:11 UT up to 00:38 UT (19:35 LT–21:00 LT). The severity of the scintillation occurrences follows the NmF2 profiles, and the resemblance between the increases in both quantities is evident. Profiles for the entire set (30 nights) are provided as supplementary material (Figure_S2)

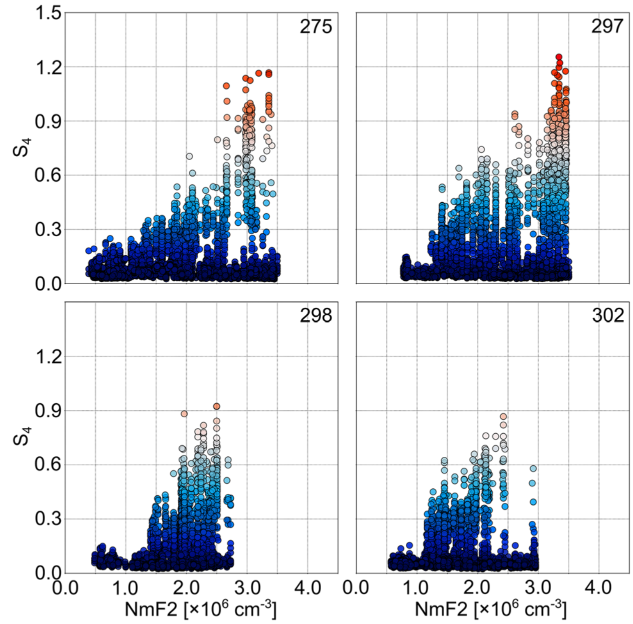

Fig. 3 S_4 values and background NmF2 at every IPP available for four example nights (indicated on the top right corner of each panel) illustrate well the relationship found between S_4 and NmF2. The blue/red circles indicate smaller/larger values. The time interval is the same as in Fig. 2. A clear connection between the two quantities can be noticed. The entire set of observations covering 30 nights is provided as supplementary material (Figure_S3)

latitudinal distribution of the magnitudes of both quantities, NmF2 and S_4, follows the same trend over all the distinct dip latitudes. In addition to that, when the peak values of NmF2 increase, the maximum values of S_4 increase as well, without changing the latitudinal trend. Therefore, there are correspondences between these quantities in both spatial distribution and magnitude.

The analysis presented next demonstrates the relation between NmF2 and S_4 from a different perspective. The procedure used was to find, for every S_4 value measured by the 6 ground-based monitors, the coordinates of the IPP and the individual background NmF2 value corresponding to those coordinates. Figure 3 shows a graphical representation of S_4 values according to the background NmF2 at the corresponding IPPs for the same nights previously discussed in Fig. 2. The colored blue/red circles indicate smaller/larger values. An increasing trend interconnecting both quantities is evident. The pattern is also coherent over distinct days. In addition, as mentioned earlier, the S_4 maximum values during nights with larger magnitudes of NmF2 are also larger.

It is worth mentioning that even under large NmF2 values, the S_4 also depends on the presence of EPBs over the station. Consequently, Figs. 2 and 3 show that increasing values of NmF2 are related to more intense scintillation severity but are not a sufficient condition. As expected, when EPBs are not present S_4 values near zero are observed. Therefore, the most adequate approach is to determine bounds of the S_4 values, that is, the maximum values of S_4 one can expect in the scenario that an EPB is present. This approach is described in the following section.

On the quantification of the relationship between the scintillation severity and the background NmF2

The objective of the analysis presented here was to verify the viability of quantifying the relation between NmF2 and the amplitude scintillation severity. Whalen (2009) used 11 days of data at a single location below the EIA peak and proposed that a linear relation can be established between the NmF2 values and the maximum level of S_4. The present study proposes the use of a larger dataset compared to that used by Whalen (2009). These preliminary results cover regions from the geomagnetic equator down to dip latitudes of 23.71° S during a period of 30 days, as mentioned earlier.

An ordinary linear regression is not the best option due to the heteroskedastic characteristic found in the dataset; instead, a procedure usually referred to as quantile regression was employed (Hall and Sheather 1988; Koenker and Bassett 1978; Eide and Showalter 1998; Cade and Noon 2003;

Koenker 2005; Wei et al. 2006; Beyerlein 2014; Das et al. 2019). While linear regression uses ordinary least squares estimators ($\hat{\beta}$) that minimize the sum of square residuals, the coefficients in the conditional quantile $[Q_\tau(y_i|x_i) = x_i\beta_\tau]$, for the τth quantile, are obtained using estimators ($\hat{\beta}_\tau$) that minimize, instead, the sum of weighted absolute residuals:

$$\sum_{i:y_i \geq x_i\hat{\beta}_\tau}^{N} \tau\left|y_i - x_i\hat{\beta}_\tau\right| + \sum_{i:y_i < x_i\hat{\beta}_\tau}^{N} (1-\tau)\left|y_i - x_i\hat{\beta}_\tau\right| \tag{2}$$

where for $i = 1,\ldots,N$, x (predictor) is the independent variable, and y (outcome) is the dependent variable. To absolute values of positive/negative residuals are applied weights of τ and 1-τ, respectively. Using this method and considering the quantile 0.99 (i.e., the 99th percentile) it is possible to determine a first-order polynomial beneath which 99% of the scintillation events are concentrated, i.e., the S_4 severity can be "bounded" by a line corresponding to the maximum S_4 as a function of the NmF2 value. In addition, the amplitude scintillation is known to saturate when the standard deviation and the average of the signal intensity are contiguous, typically reaching values of, at most, 1.3 (Basu et al. 1996; Forte and Radicella 2002). Therefore, S_4 is not expected to increase linearly with NmF2 indefinitely. To properly address these aspects, the natural logarithm was applied to the NmF2 values before the calculation of the quantile regression. The procedure was performed considering all the S_4 values and the corresponding NmF2 values at the same IPPs for every night (for all the IPPs where $S_4 \geq 0.2$) to produce a general expression. Applying the bootstrap technique (Hesterberg 2011) on the measurement samples (38,022 values), the estimated standard error was 0.022, with corresponding p-value = 0. This indicates that the representation by the model is statistically significant. More essential is the fact that the approach is suitable to ensure that 99% of the scintillation is bounded by the estimated curve.

Figure 4 shows the result using the entire dataset (blue/red circles) and the corresponding quantile regression (99th percentile) (black solid line). For comparison purposes, the approximation provided by Whalen (2009) is also depicted (green line). The values of maximum S_4 [$S_{4\,(max)}$] as a function of NmF2 (in cm^{-3}) can then be determined by:

$S_{4\,(max)} = -5.79 + 0.46 \times \ln(\text{NmF2})$. (3).

The relation in (3) can now be used to estimate $S_{4\,(max)}$ one can expect when EPBs occur, for a given condition of background NmF2. To demonstrate the performance of the proposed approach, Fig. 5 shows amplitude scintillation measurements (blue/red circles) and estimated $S_{4\,(max)}$ (solid lines) using Eq. 3. Each line corresponds to a magnetic meridian described in Fig. 1 and presented also in Fig. 2. The panels on the left show results for nights from the dataset (days of year 280, 287, and 290, i.e., October 7, 14, and 17, 2022) that were used to produce (3). These results are shown to demonstrate that, as expected, the derived model is consistent with the data used, and that 99% of the scintillation lies beneath the $S_{4\,(max)}$ curve for every dip latitude considered. The panels on the right of Fig. 5, on the other hand, show results for the nights of March 13, 18, and November 8, 2022 (days of year 72, 77, and 312, respectively), which were months outside the dataset used to derive (3) but have similar solar flux conditions and longitudes.

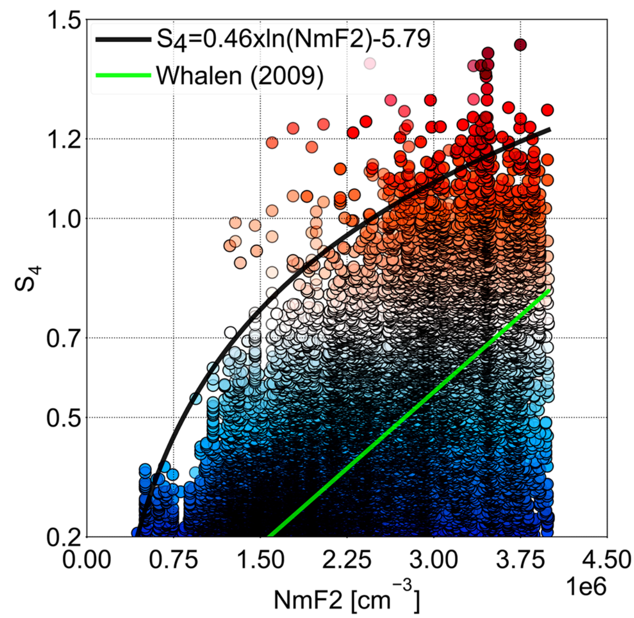

Fig. 4 Relation between S_4 values and NmF2 considering every IPP available in the entire dataset ($S_4 \geq 0.2$). The blue/red circles indicate smaller/larger values. The black solid line corresponds to the general quantile regression "bounding" the 99th percentile of the S_4 activity. The green line corresponds to the results using the approach of Whalen (2009). The time interval is the same as in Fig. 2

The results shown on the left side of Fig. 5 illustrate the performance and adequacy of the relation in (3). The results in the right-side panels of Fig. 5 also show the appropriateness of the procedure when estimating scintillation severity for different months, but similar solar flux and longitudes (and similar LT). In addition, each of the 3 nights had dissimilar NmF2 values and distinct dip latitudes for the NmF2 peak, allowing the approach to be tested in different background conditions. It is evident from Fig. 5 that the estimated $S_{4\,(max)}$ exhibits a close resemblance with the trend in the measured S_4 values and that (3) provides satisfactory estimates of maximum scintillation severity, with very few deviations (below 1% of the data). Therefore, it would be possible to estimate expected maximum scintillation levels in case of EPB occurrence at a location where background NmF2 is available, as proposed by Whalen (2009).

It is worth reminding the reader that if EPBs are absent, scintillation would not be observed even under conditions

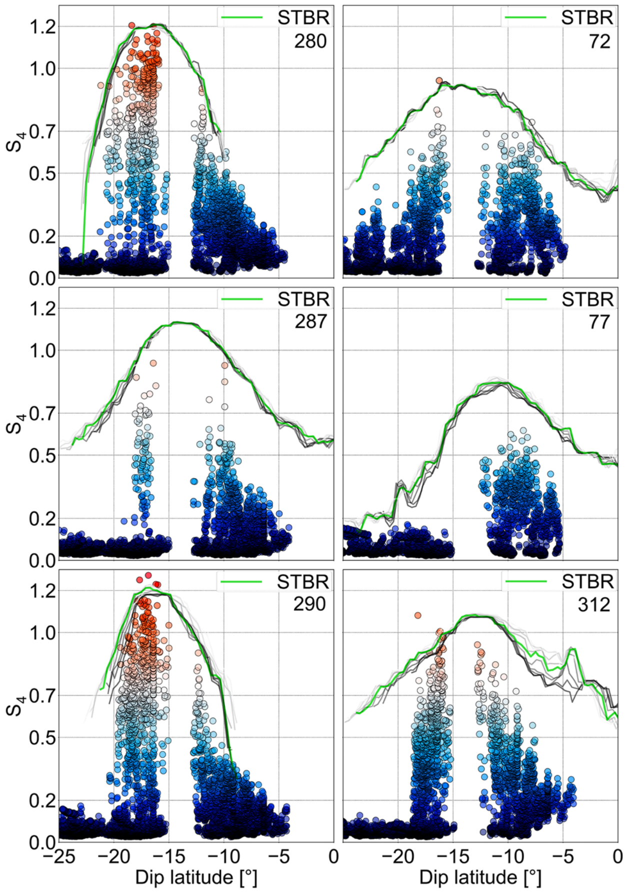

Fig. 5 Comparison between real amplitude scintillation (blue/red circles) and estimated $S_{4\,(\mathrm{max})}$ (colored lines). Left panels: 3 nights from the dataset (280, 287, and 290, 2022) used in the derivation of (3). Right panels: 3 arbitrarily chosen nights (72, 77, and 312, 2022) outside the dataset used to produce (3). These panels demonstrate the suitableness of the approach to describe the scintillation severity for any night of interest. The general trend described by the estimated $S_{4\,(\mathrm{max})}$ is clearly in good agreement with the real data. Also, $S_{4\,(\mathrm{max})}$ is "bounding" at least 99% of the data, i.e., the measured S_4 values are essentially underneath the predicted curves over all the dip latitudes evaluated. The time interval is the same as in Fig. 2

of large NmF2. This is illustrated in Figure S2, which shows that not all measurements of large NmF2 are accompanied by measurements of elevated S_4. One would be inclined to think that the model would overestimate $S_{4\,(\mathrm{max})}$. This is not correct since $S_{4\,(\mathrm{max})}$ represents the maximum S_4 one can expect for a given condition of background NmF2. This is important since estimates of background NmF2 are becoming more available (e.g., GOLD) but tracking the occurrence and spatiotemporal variability of EPBs is still a challenge. Therefore, this work describes an approach for obtaining an upper bound for S_4.

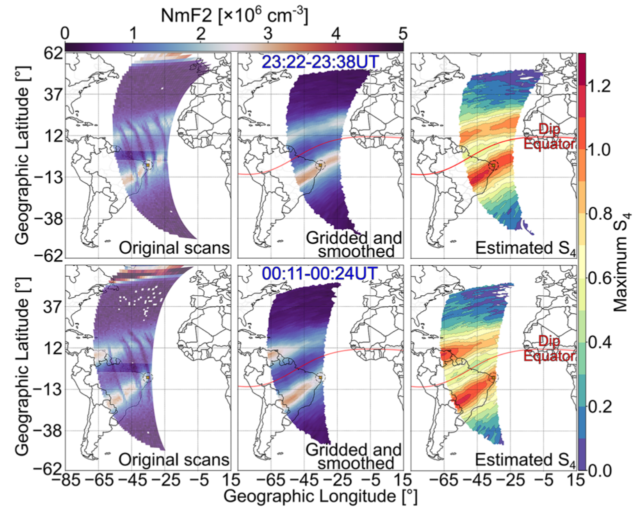

Fig. 6 Scintillation severity map using GOLD NMAX (NmF2) data and the relation given by (3). Top panels: original scans from GOLD (left), gridded and smoothed NmF2 (middle), and estimated scintillation severity, $S_{4\,(\mathrm{max})}$ (right) for 23:22 UT–23:38 UT. Bottom panels: Original scans from GOLD (left), gridded and smoothed NmF2 (middle), and estimated scintillation severity, $S_{4\,(\mathrm{max})}$ (right) for 00:11 UT–00:24 UT

On the use of the relationship between the $S_{4\,(\mathrm{max})}$ and NmF2 to produce scintillation severity maps

A relationship such as (3) could be used with space-based measurements to generate maps of potential maximum scintillation. The procedure proposed here is to apply the relationship to every NmF2 measurement available, generating a higher-level data product. To illustrate this idea and provide insight on the feasibility and performance of the potential approach, data from a scintillation ground-based monitor deployed at the Brazilian eastern coast (STNT) was used. Data from this monitor was not used to produce the empirical $S_{4\,(\mathrm{max})}$-NmF2 relationship (3). Additionally, it is at least 14° to the east of any of the 6 monitors whose data were used in the derivation of (3). Table 1 and Fig. 1 can be inspected for more details.

Figure 6 shows the results for October 14, 2022 (day of year 287), considering 4 GOLD scans covering time intervals separated by approximately 50 min. The date is well within the range of dates from which data was used to create the $S_{4\,(\mathrm{max})}$-NmF2 empirical relationship. Therefore, it is possible to assess the performance of the proposed approach for measurements made at a different longitude sector but similar season and solar flux conditions. The first two scans started at 23:22 UT and ended at 23:38 UT, the final two scans started at 00:11 UT and ended at 00:24 UT. For the STNT station, these UTs correspond to approximately 21:01 LT–21:17 LT and 21:50 LT–22:03 LT, respectively,

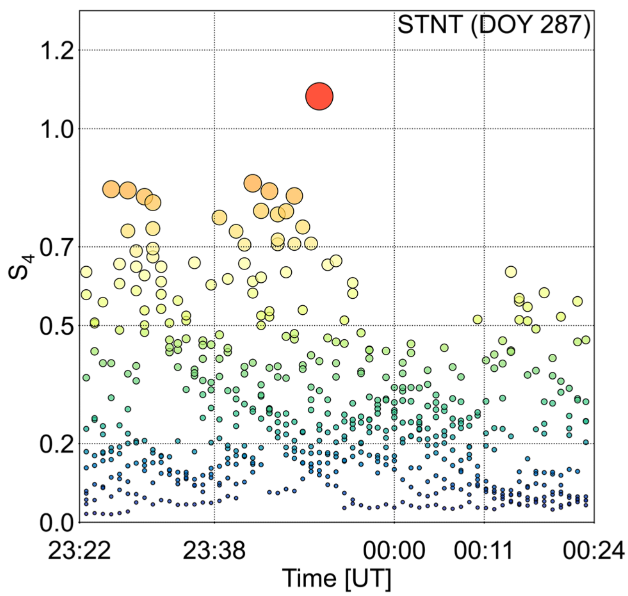

Fig. 7 Real scintillation data recorded at STNT station on October 14, 2022 (day of year 287). The maximum S_4 observed in the intervals 23:22 UT–23:38 UT and 00:11 UT–00: 24 UT are, respectively, 0.85 and 0.64

i.e., early nighttime, when scintillation is expected to occur (Sousasantos et al. 2018).

The top panels exhibit the results for the first two scans between 23:22 UT and 23:38 UT. The top left panel shows the original GOLD NMAX (NmF2) data with values described by the color bar at the top. Several EPBs (blue streaks) can be readily noticed, with one exactly over the STNT station (orange "x" marker). The top middle panel exhibits the NmF2 data after the gridding and smoothing processes used to remove the electron density "bite-outs" from the background NmF2. The values are also described by the color bar at the top. The STNT elevation angle coverage (grey dashed circle) is centered in the EIA region. The top right panel shows the estimated scintillation severity [$S_{4\,(\max)}$] applying the relationship given by (3) on the NmF2 gridded and smoothed data. The values are detailed by the color bar at the right-hand side. The isocontours reveal maximum scintillation in the range $0 \leq S_{4\,(\max)} \leq 1.2$ for distinct dip latitudes. Particularly over STNT, for the time interval between 23:22 UT and 23:38 UT, the value found was $1.0 \leq S_{4\,(\max)} \leq 1.1$.

The bottom panels in Fig. 6 are similar to those on top, but this time for the scans covering regions slightly to the west and between 00:11 UT and 00:24 UT. A different EPB (bottom left panel) is again over STNT, but the background NmF2 (bottom middle panel) decreased in comparison with the top middle panel, consequently, the estimated maximum scintillation in the STNT field-of-view varied in the ranges $0.9 \leq S_{4\,(\max)} \leq 1.0$ and $1.0 \leq S_{4\,(\max)} \leq 1.1$.

Figure 7 shows real scintillation data from STNT station for the same night (October 14, 2022, i.e., day of year 287), with the same elevation angles (≥ 45°), and at the same time interval. The colors (and the sizes) of the circles are related to the S_4 values and are the same as used in Fig. 6. Between 23:22 UT and 23:38 UT, when GOLD-based estimates predicted $1.0 \leq S_{4\,(\max)} \leq 1.1$ for the field-of-view of the STNT station, maximum values of S_4 measured by the monitor were 0.85 (at 23:26 UT). Between 00:11 UT and 00:24 UT, on the other hand, when GOLD-based estimates predicted $0.9 \leq S_{4\,(\max)} \leq 1.1$ for the field-of-view of the STNT station, the monitor at the station measured a maximum S_4 value of 0.64 (at 00:14 UT). Therefore, the estimated $S_{4\,(\max)}$ values in Fig. 6 are in good conformity with the observations, providing adequate maximum boundaries of scintillation severity. It must be pointed out that Fig. 7 shows a S_4 value reaching 1.08 at 23:51 UT. While the scans exhibited in Fig. 6 do not cover this particular time, both, prior and subsequent scans show estimated $S_{4\,(\max)}$ values that also bound that scintillation level.

Concluding remarks

Previous studies have already shown that scintillation severity is enhanced around the EIA peaks, and that the background ionospheric F-region density controls the scintillation severity. This work proposes that collocated and spatially distributed observations of NmF2 and S_4 can be used to quantify the relationship between the background F-region peak electron density and the scintillation severity. NMAX (NmF2) images from the GOLD instrument and amplitude scintillation data (S_4 indices) from 6 ground-based monitors deployed over the Brazilian region were used to evaluate the feasibility of this approach.

The analyses started by examining the dependence of the scintillation severity on the peak electron density over distinct dip latitudes. The results demonstrated a remarkable similarity in the latitudinal variation of background NmF2 and S_4.

After that, the S_4 values obtained from scintillation monitors deployed along the same geomagnetic meridian were compared with NmF2 values at the corresponding IPPs. The results showed a noticeable coherent pattern between the two quantities (background NmF2 and S_4).

A relation between maximum S_4 [$S_{4\,(\max)}$] and background NmF2 values was quantified using a quantile (99th percentile) regression approach. $S_{4\,(\max)}$ represents the upper bound in S_4 for a given condition of background NmF2. The empirical relationship (3) was successfully evaluated using independent GOLD and scintillation measurements.

The empirical relationship was also used to produce $S_{4\,(\max)}$ maps derived from GOLD NMAX (NmF2) observations. The performance of these maps was tested using an additional ground-based monitor located approximately 14° to the east of all other monitors whose data was used in the quantile calculation. The results show good estimates of $S_{4\,(\mathrm{max})}$.

The main conclusions can be summarized as follows:

(1) A comparison between GOLD NMAX (NmF2) and ground-based L-band scintillation data shows that background NmF2 plays an important role in scintillation severity. It shows how the latitudinal and day-to-day variability of the EIA controls the variability of $S_{4\,(\mathrm{max})}$.
(2) Using collocated GOLD NmF2 and scintillation measurements, it was shown that an empirical description of $S_{4\,(\mathrm{max})}$ based on background NmF2 can be obtained. Using independent measurements, the performance of the empirical relationship for estimating $S_{4\,(\mathrm{max})}$ from NmF2 was illustrated.
(3) The results indicate the possibility of using empirical relationships between background NmF2 and $S_{4\,(\mathrm{max})}$, such as the one derived in this work, to create $S_{4\,(\mathrm{max})}$ maps from GOLD-like observations. It must be emphasized that $S_{4\,(\mathrm{max})}$ represents the maximum S_4 one could expect for a given condition of background NmF2 and EPB occurrence. This is important since distributed estimates of NmF2 (e.g., GOLD) are becoming more available, but the specification of the occurrence and spatiotemporal variability of EPBs is still a challenge.

This work focused on deriving a relationship between NmF2 and $S_{4\,(\mathrm{max})}$ for a specific local time (19:35 LT–21:00 LT) and longitude sector (western Brazil) employing a limited dataset of collocated observations. The results, nevertheless, showed the feasibility of the proposed approach, demonstrating the connection between the values of NmF2 and the scintillation severity. The advantage of this approach is that it only uses the NmF2 and S_4 observations, not requiring the specification of processes causing the NmF2 variability, etc. As an illustration of potential application, cases of scintillation severity maps were presented and evaluated using independent GOLD and scintillation observations (different longitude sector, but similar solar flux, year/month, and LT) with encouraging results.

Finally, it must be mentioned that the relationship presented here (3) may not be well-suited for geophysical conditions and locations considerably distinct from those analyzed in this study. For instance, future work will investigate to what extent the relationship is valid to other local times and/or longitude sectors. Future work might also address using data from other instruments or measurement techniques for creating or evaluating relationships between scintillation severities and background plasma densities.

Supplementary Information The online version contains supplementary material available at https://doi.org/10.1007/s10291-023-01602-6.

Acknowledgements Research at UT Dallas was supported by NSF awards AGS-1916055 and AGS-2122639. A. O. Moraes is grateful to CNPq (309389/2021-6). R. W. Eastes was supported by NASA contract 80GSFC18C0061 to the University of Colorado. J. F. G. Monico acknowledges CNPq (304773/2021-2). Authors would like to thank the International Association of Geomagnetism and Aeronomy (IAGA) and all the scientific and technical staff responsible for the distribution of the International Geomagnetic Reference Field (IGRF). Projects CIGALA/CALIBRA were funded by the European Commission (EC) in the framework of awards FP7-GALILEO-2009-GSA and FP7–GALILEO–2011–GSA–1a, as well of FAPESP award 06/04008-2. INCT NavAer is supported by CNPq (465648/2014-2) and FAPESP (2017/50115-0). GOLD is supported by NASA contract 80GSFC18C0061 to the University of Colorado.

Author contributions JSS contributed with processing of the observations, writing of the manuscript, figures, and interpretation of the results. FSR proposed the study and contributed with interpretation of the results and writing of the manuscript. AOM contributed with processing, interpretation of scintillation data and writing of the manuscript. RWE curated the GOLD data and contributed with the writing of the manuscript. JFGM curated the scintillation data and writing of the manuscript. All authors reviewed the manuscript.

Data availability The GOLD data is available at the GOLD Science Data Center (https://gold.cs.ucf.edu/data/search/) and at the NASA Space Physics Data Facility (https://spdf.gsfc.nasa.gov/). The IGRF13 used to calculate geomagnetic components is available at https://www.ngdc.noaa.gov/IAGA/vmod/igrf.html. The scintillation data is available at https://ismrquerytool.fct.unesp.br/is/#.

Declarations

Competing interests The authors declare no competing interests.

References

Aarons J (1982) Global morphology of ionospheric scintillations. Proc IEEE 70(4):360–378. https://doi.org/10.1109/PROC.1982.12314
Affonso BJ, Moraes AO, Sousasantos J, Marini-Pereira L, Pullen S (2022) Strong ionospheric spatial gradient events induced by signal propagation paths aligned with equatorial plasma bubbles. IEEE Trans Aerosp Electron Syst 58(4):2868–2879. https://doi.org/10.1109/TAES.2022.3144622
Alken P et al (2021) International geomagnetic reference field: the thirteenth generation. Earth, Planets Space 73(49):1–25. https://doi.org/10.1186/s40623-020-01288-x
Basu S, Groves KM (2001) Specification and forecasting of outages on satellite communication and navigation systems. Washington DC Am Geophys Union Geophys Monogr Ser 125:423–430. https://doi.org/10.1029/GM125p0423
Basu S et al (1996) Scintillations, plasma drifts, and neutral winds in the equatorial ionosphere after sunset. J Geophys Res Space Phys 101(A12):26795–26809. https://doi.org/10.1029/96JA00760
Basu S, Basu S, Huba J, Krall J, McDonald SE, Makela JJ, Miller ES, Ray E, Groves K (2009) Day-to-day variability of the equatorial ionization anomaly and scintillations at dusk observed by GUVI and modeling by SAMI3. J Geophys Res Space Phys 114(A4):1–12. https://doi.org/10.1029/2008JA013899

Batista, IS, Diogo EM, Souza JR, Abdu MA, Bailey GJ (2011) Equatorial ionization anomaly: the role of thermospheric winds and the effects of the geomagnetic field secular variation. In: aeronomy of the earth's atmosphere and ionosphere, pp 317–328. Springer, Dordrecht. https://doi.org/10.1007/978-94-007-0326-1_23.
Beyerlein A (2014) Quantile regression: opportunities and challenges from a user's perspective. Am J Epidemiol 180(3):330–331. https://doi.org/10.1093/aje/kwu178
Briggs BH, Parkin IA (1963) On the variation of radio star and satellite scintillations with zenith angle. J Atmos Terr Phys 25(6):339–366. https://doi.org/10.1016/0021-9169(63)90150-8
Cade BS, Noon BR (2003) A gentle introduction to quantile regression for ecologists. Front Ecol Environ 1(8):412–420. https://doi.org/10.1890/1540-9295(2003)001[0412:AGITQR]2.0.CO;2
Das K, Krzywinski M, Altman N (2019) Quantile regression. Nat Methods 16(6):451–452. https://doi.org/10.1038/s41592-019-0406-y
de Paula ER, Rodrigues FS, Iyer KN, Kantor IJ, Abdu MA, Kintner PM, Ledvina BM, Kil H (2003) Equatorial anomaly effects on GPS scintillations in Brazil. Adv Space Res 31(3):749–754. https://doi.org/10.1016/S0273-1177(03)00048-6
de Paula ER, Monico JFG, Tsuchiya IH, Valladares CE, Costa SMA, Marini-Pereira L, Vani BC, Moraes AO (2023) A retrospective of global navigation satellite system ionospheric irregularities monitoring networks in Brazil. J Aerosp Technol Manag 15(e0123):1–17. https://doi.org/10.1590/jatm.v15.1288
Eastes RW et al (2017) The global-scale observations of the limb and disk (GOLD) mission. Space Sci Rev 212:383–408. https://doi.org/10.1007/s11214-017-0392-2
Eastes RW, Solomon SC, Daniell RE, Anderson DN, Burns AG, England SL, Martinis CR, McClintock WE (2019) Global-scale observations of the equatorial ionization anomaly. Geophys Res Lett 46(16):9318–9326. https://doi.org/10.1029/2019GL084199
Eide E, Showalter MH (1998) The effect of school quality on student performance: a quantile regression approach. Econ Lett 58(3):345–350. https://doi.org/10.1016/S0165-1765(97)00286-3
Flynn CD, McCaffrey AM, Jayachandran PT, Langley RB (2019) Discovery of new code interference phenomenon in GPS observables. GPS Solut 23(65):1–9. https://doi.org/10.1007/s10291-019-0858-7
Forte B, Radicella SM (2002) Problems in data treatment for ionospheric scintillation measurements. Radio Sci 37(6):8-1–8-5. https://doi.org/10.1029/2001RS002508
Hall P, Sheather SJ (1988) On the distribution of a studentized quantile. J Roy Stat Soc: Ser B (methodol) 50(3):381–391. https://doi.org/10.1111/j.2517-6161.1988.tb01735.x
Hesterberg T (2011) Bootstrap. Wiley Interdiscip Rev Comput Stat 3(6):497–526. https://doi.org/10.1002/wics.182
Kelley MC, Larsen MF, La Hoz C (1981) Gravity wave initiation of equatorial spread F: a case study. J Geophys Res 86(A11):9087–9100. https://doi.org/10.1029/JA086iA11p09087
Khadka SM, Valladares CE, Sheehan R, Gerrard AJ (2018) Effects of electric and neutral wind on the asymmetry of equatorial ionization anomaly. Radio Sci 53(5):683–697. https://doi.org/10.1029/2017RS006428
Koenker R (2005) Quantile regression (econometric society monographs). Cambridge University Press, Cambridge. https://doi.org/10.1017/CBO9780511754098
Koenker R, Bassett G Jr (1978) Regression quantiles. Econometrica 46(1):33–50. https://doi.org/10.2307/1913643
Lou S, Jiang X, Scott PJ (2013) Geometric computation theory for morphological filtering on freeform surfaces. Proc R Soc Lond Math Phys Eng Sci 469(2159):20130150. https://doi.org/10.1098/rspa.2013.0150
McClintock WE et al (2020) Global-scale observations of the limb and disk mission implementation: 2. Observations, data pipeline, and level 1 data products. J Geophys Res Space Phys 125(5):1–16. https://doi.org/10.1029/2020JA027809
Monico JFG et al (2022) The GNSS NavAer INCT project overview and main results. J Aerosp Technol Manag 14(e0722):1–23. https://doi.org/10.1590/jatm.v14.1249
Monico JFG, Camargo PO, Alves DBM, Shimabukuro MH, Aquino M, Pereira VAS, Vani BC (2013) From CIGALA to CALIBRA: an infrastructure for ionospheric scintillation monitoring in Brazil. In: AGU meeting of Americas in Cancun.
Moraes AO, Costa E, Abdu MA, Rodrigues FS, de Paula ER, Oliveira K, Perrella WJ (2017) The variability of low-latitude ionospheric amplitude and phase scintillation detected by a triple-frequency GPS receiver. Radio Sci 52(4):439–460. https://doi.org/10.1002/2016RS006165
Moraes AO, Muella MTAH, de Paula ER, Oliveira CBA, Terra WP, Perrella WJ, Meibach-Rosa PRP (2018a) Statistical evaluation of GLONASS amplitude scintillation over low latitudes in the Brazilian territory. Adv Space Res 61(7):1776–1789. https://doi.org/10.1016/j.asr.2017.09.032
Moraes AO et al (2018b) GPS availability and positioning issues when the signal paths are aligned with ionospheric plasma bubbles. GPS Solut 22(4):1–12. https://doi.org/10.1007/s10291-018-0760-8
Moraes AO, Vani BC, Costa E, Sousasantos J, Abdu MA, Rodrigues FS, Gladek YC, de Oliveira CBA, Monico JFG (2018c) Ionospheric scintillation fading coefficients for the GPS L1, L2, and L5 frequencies. Radio Sci 53(9):1165–1174. https://doi.org/10.1029/2018RS006653
Reinisch BW, Bibl K, Kitrosser DF, Sales GS, Tong JS, Zahn ZM, Bullett TW, Rails JA (1989) The Digisonde 256 ionospheric sounder. In: Liu, C. H. (eds.) World ionosphere/thermosphere study. WITS Handbook, vol 2, pp 350–366. SCOSTEP, IL
Rodrigues FS, Socola JG, Moraes AO, Martinis C, Hickey DA (2021) On the properties of and ionospheric conditions associated with a mid-latitude scintillation event observed over southern United States. Space Weather 19(6):1–20. https://doi.org/10.1029/2021SW002744
Salles LA, Moraes AO, Vani BC, Sousasantos J, Affonso BJ, Monico JFG (2021) A deep fading assessment of the modernized L2C and L5 signals for low-latitude regions. GPS Solut 25(122):1–13. https://doi.org/10.1007/s10291-021-01157-4
Smith JM, Heelis RA (2018a) The plasma environment associated with equatorial ionospheric irregularities. J Geophys Res Space Physics 123(2):1583–1592. https://doi.org/10.1002/2017JA024933
Smith JM, Heelis RA (2018b) Plasma dynamics associated with equatorial ionospheric irregularities. Geophys Res Lett 45(16):7927–7932. https://doi.org/10.1029/2018GL078560
Sobral JHA, Abdu MA, Takahashi H, Taylor MJ, de Paula ER, Zamlutti CJ, de Aquino MG, Borba G (2002) Ionospheric plasma bubble climatology over Brazil based on 22 years (1977–1998) of airglow observations. J Atmos Solar Terr Phys 64(12–14):1517–1524. https://doi.org/10.1016/S1364-6826(02)00089-5
Sousasantos J, Moraes AO, Sobral JHA, Muella MTAH, de Paula ER, Paolini RS (2018) Climatology of the scintillation onset over southern Brazil. Ann Geophys 36(2):565–576. https://doi.org/10.5194/angeo-36-565-2018
Sousasantos J, Abdu MA, de Paula ER, Moraes AO, Salles LA, Affonso BJ (2022a) Conjugated asymmetry of the onset and magnitude of GPS scintillation driven by the vertical plasma drift. GPS Solut 26(75):1–13. https://doi.org/10.1007/s10291-022-01258-8
Sousasantos J, Affonso BJ, Moraes AO, Rodrigues FS, Abdu MA, Salles LA, Vani BC (2022b) Amplitude scintillation severity and fading profiles under alignment between GPS propagation paths and equatorial plasma bubbles. Space Weather 20(11):1–15. https://doi.org/10.1029/2022SW003243
Sousasantos J, Gomez Socola J, Rodrigues FS, Eastes RW, Brum CGM, Terra P (2023) Severe L-band scintillation over low-to-mid

latitudes caused by an extreme equatorial plasma bubble: joint observations from ground-based monitors and GOLD. Earths Planets Space 75(41):1–12. https://doi.org/10.1186/s40623-023-01797-5
Sternberg SR (1983) Biomedial image processing. Computer 16(1):22–34. https://doi.org/10.1109/MC.1983.1654163
Vani BC, Forte B, Monico JFG, Skone S, Shimabukuro MH, Moraes AO, Portella IP, Marques HA (2019) A novel approach to improve GNSS precise point positioning during strong ionospheric scintillation: theory and demonstration. IEEE Trans Veh Technol 68(5):4391–4403. https://doi.org/10.1109/TVT.2019.2903988
Vani BC, Moraes AO, Salles LA, Breder, VHF, Freitas MJS, Monico JFG, de Paula ER (2021) Monitoring ionospheric scintillations with GNSS in South America: Scope, results, and challenges. In: GPS and GNSS technology in geosciences, pp 255–280, Elsevier. https://doi.org/10.1016/B978-0-12-818617-6.00012-3.
Wei Y, Pere A, Koenker R, He X (2006) Quantile regression methods for reference growth charts. Stat Med 25(8):1369–1382. https://doi.org/10.1002/sim.2271
Whalen JA (2009) The linear dependence of GHz scintillation on electron density observed in the equatorial anomaly. Ann Geophys 27(4):1755–1761. https://doi.org/10.5194/angeo-27-1755-2009
Yeh KC, Liu CH (1982) Radio wave scintillations in the ionosphere. Proc IEEE 70(4):324–360. https://doi.org/10.1109/PROC.1982.12313
Yousuf M, Dashora N, Sridhar M, Dutta G (2023) Long-term impact of ionospheric scintillations on kinematic precise point positioning: seasonal and solar activity dependence over Indian low latitudes. GPS Solut 27(40):1–12. https://doi.org/10.1007/s10291-022-01378-1

J. Sousasantos graduated in Mathematics from the Universidade de Taubaté, Brazil, in 2010. M. Sc. (2013) and Dr. Sc. (2017) degrees obtained at the Instituto Nacional de Pesquisas Espaciais (INPE). He is currently a research associate at the University of Texas in Dallas. His areas of interest are mathematical modeling and forecasting of ionospheric irregularities, scintillation, and atmospheric-ionospheric vertical coupling.

F. S. Rodrigues has BS in Electrical Engineering (Universidade Federal de Santa Maria, 2001), M. Sc. in Space Sciences (INPE, 2003), and a Ph.D. in Electrical and Computer Engineering (Cornell University, 2008). He is currently an associate professor at The University of Texas at Dallas. Some of his areas of interest are the development and application of remote sensing techniques for fundamental and applied studies of the upper atmosphere, numerical modeling studies of the thermosphere and ionosphere, and studies of ionospheric irregularity effects on signals used by Global Navigation Satellite Systems (GNSS).

A. O. Moraes received a BS in telecommunications engineering from Universidade de Taubaté (2003), and Dr. Sc. from the Instituto Tecnológico de Aeronáutica (2013) and has been a technologist at the Instituto de Aeronáutica e Espaço since 2004 and graduate professor since 2015.

R. W. Eastes is a research scientist at the Laboratory for Atmospheric and Space Physics (LASP) at the University of Colorado Boulder. He is the principal investigator (PI) of the Global-scale Observations of the Limb and Disk (GOLD) mission. In 2019 he was awarded with the Exceptional Public Service Medal, conferred by National Aeronautics and Space Administration (NASA).

J. F. G. Monico graduated in Cartographic Eng. from UNESP (1982), a Master in Geodetic Science from UFPR (1988), and a Ph.D. in Space Geodesy from Nottingham University (1995). He has experience in geosciences, focusing on the following subjects: GNSS for Geodesy and Atmosphere, Quality Control on Geodesy.